Journal of Materials Chemistry A

Cross-linked Perovskite/Polymer using Sodium Borate Composites for Efficient and Stable Perovskite Solar Cells

Journal:	*Journal of Materials Chemistry A*
Manuscript ID	TA-ART-03-2022-002565.R1
Article Type:	Paper
Date Submitted by the Author:	31-May-2022
Complete List of Authors:	Jo, Bonghyun; Sungkyunkwan University - Suwon Campus, School of Advanced Materials Science and Engineering; Sungkyunkwan University - Suwon Campus, SKKU Institute of Energy Science and Technology (SIEST) Han, Gill Sang; Sungkyunkwan University - Suwon Campus, School of Advanced Materials Science and Engineering; Sungkyunkwan University - Suwon Campus, SKKU Institute of Energy Science and Technology (SIEST) Yu, Hyang Mi; Sung Kyun Kwan University College of Natural Science, Energy Science Choi, Jin Hyuk ; Sungkyunkwan University, School of Advanced Materials Science and Engineering Zhu, Jun; Sungkyunkwan University College of Natural Science, Energy Science Ahn, Tae; Sungkyunkwan University - Suwon Campus, Energy Science; Korea Research Institute of Chemical Technology, 141 Gajeong-ro, Yuseong-gu Gon, Namkoong; Old Dominion University, Electrical and Computer Engieering Jung, Hyun Suk; Sungkyunkwan University - Suwon Campus, School of Advanced Materials Science and Engineering; Sungkyunkwan University - Suwon Campus, SKKU Institute of Energy Science and Technology (SIEST)

Cross-linked Perovskite/Polymer using Sodium Borate Composites for Efficient and Stable Perovskite Solar Cells

Received 00th March 20xx,
Accepted 00th March 20xx

DOI: 10.1039/x0xx00000x

Bonghyun Jo[a,b]†, Gill Sang Han[a,b]†, Hyang Mi Yu[c], Jinheok Choi[a], Jun Zhu[a,c], Tae Kyu Ahn[c], Gon Namkoong[c,d]* and Hyun Suk Jung[a,b]*

Although perovskite solar cells have been widely investigated to improve the photovoltaic conversion efficiency so far, perovskite light absorbers have a severe disadvantage for commercialization due to their facile degradation when exposed to humidity and oxygen. Herein, we suggest a synergic anti-solvent dripping strategy to improve the performance and stability of a photovoltaic device using a mixture of PMMA/sodium borate salt (borax) and perovskite materials. We characterized its unique features, i.e., the enhanced hydrogen bond formation between the PMMA/sodium borate mixture and perovskite light absorber, which induced the lateral grain growth of perovskite films and the efficient passivation of the surface and grain boundary. Consequently, the PMMA/borax-treated devices exhibited significantly improved efficiency from 20.93% to 22.05% and retained 80% of the initial device performance over 1084 h at 22 °C and 50% RH. We believe this technology will be useful for commercializing various optoelectronic devices.

1. Introduction

Hybrid organic-inorganic perovskite materials have been attributed to boost device power conversion efficiency through their outstanding optoelectronic and photophysical properties, revolutionizing the photovoltaic field owing to their simple fabrication via the solution-casting process.[1] Since the state-of-the-art perovskite solar cell (PSC) demonstrated a decent power conversion efficiency (PCE) of 25.7%, various strategies have been proposed to open further chance to achieve alleviated performance close to its Schockley-Queisser (SQ) limit of approximately 33%.[2,3] Notably, it has been observed that defects located at grain boundaries (GBs) between neighboring grains or the interfaces between polycrystalline perovskite films in combination with charge-transporting layers act as trap centers and are the main sources of performance loss for PSCs. Furthermore, perovskite films are prepared by the solvent processing method, which is typically prone to form defects on the film surface and GBs. These defects accelerate the degradation of perovskite and serve as nonradiative charge recombination centers that negatively impact device performance. Therefore, obtaining excellent surface coverage for perovskite film formation and enlarged crystal size for GB reduction have been considered one of the best approaches for yielding high-performing PSCs with high efficiency and stability by reducing the trap density.[4,5]

There are several approaches to improve the performance of PSCs, such as composition engineering of the perovskite materials and additive engineering of the perovskite precursor.[6,7] The compositional engineering approach, including the use of triple or quadruple cations, the chemical modification of the X site anions of Br or Cl ions, and the inclusion of various metal halide salts in the perovskite precursor for reducing defects and manipulating film morphology, has been the method of choice to date.[8,9] In addition, the inclusion of alkali salts like Li+, Na^+, K^+, and Rb^+ has been adopted as an attractive strategy to achieve highly uniform grains for enhancing stability by partially replacing formamidinium (FA^+) or methylammonium (MA^+) with these ions.[10,11,12]

Various additive materials like Lewis acid or base groups, including small molecules, and long-chain polymers, have been investigated to blend throughout the entire perovskite absorber to boost its performance and humidity tolerance. In particular, long-chain polymers have been successfully introduced; these include poly vinyl alcohol (PVA)[13], poly ethylene glycol(PEG)[14], polystyrene sulfonate (PSS)[15], poly

[a] School of Advanced Materials Science and Engineering, Sungkyunkwan University, Suwon 16419, Republic of Korea.
[b] SKKU Institute of Energy Science and Technology (SIEST), Sungkyunkwan University, Suwon 16419, Republic of Korea
[c] Department of Energy Science, Sungkyunkwan University, Suwon 16419, Republic of Korea.
[d] Department of Electrical and Computer Engineering, Old Dominion University, Norfolk, USA
*Corresponding authors: E-mail: hsjung1@skku.edu (Hyun Suk Jung); gnamkoon@odu.edu (Gon Namkoong)
† These authors contributed equally to this work.
Electronic Supplementary Information (ESI) available: [details of any supplementary information available should be included here]. See DOI: 10.1039/x0xx00000x

[(9,9-bis(3'-(N,N-dimethylamino)propyl)-2,7-fluorene)-alt-2,7-(9,9-dioctylfluorene)] (PFN)[16], and poly methyl methacrylate (PMMA).[17–19] These polymers retard crystal growth via hydrogen bonding interactions to fabricate pin-hole-free perovskite films, having large and uniform grain size as well as a barrier to protect them from hydrolytic degradation. In addition, polymers with hygroscopic properties, *e.g.,* PMMA and PVA, exhibit self-healing functionality to achieve the long-term operational stability and humidity resistance required for a marketable product. The binding effect of enhanced hydrogen bonding significantly affects perovskite stability by preventing decomposed ingredients from leaking. Thus, the ingredients recrystallize into perovskite crystals through self-healing.

Herein, we propose a synergetic strategy to improve the performance of PSCs using a PMMA/sodium borate salt (borax) mixture in an anti-solvent. Borax, also known as sodium tetraborate, is an inorganic salt composed of a boron compound ($Na_2B_4O_7$), widely used as a household cleaner and laundry detergent. In particular, borate salts with diols provided a very useful means of enhancing crosslinking functionality with other polymers. For instance, in the PVA/borax system, the borax behaved as a cross-linking agent and self-healing enhancer by cross-linking the functional groups of PVA chains via the di-diol bonds to form a viscoelastic network.[20]

In this study, PMMA/sodium borate mixtures are investigated for enhanced hydrogen bonding and their impact on the structural, optical, and photovoltaic performance of perovskite solar cells. We further expect that incorporating an alkali salt inclusion method to the polymer/perovskite blend could be a feasible passivating method to optimize the long-term stability of photovoltaic applications.

2. Results and discussion

Figure 1A schematically shows preparation of the perovskite film using PMMA/borax. The PMMA polymer and borax salts were dissolved in an anti-solvent instead of a perovskite precursor (as explained in the device fabrication section in the Supporting Information). This method overcomes several methodological limitations, such as the formation of heterophases, insoluble additives, and the inappropriate miscibility of the additives in the perovskite precursor. In addition, it has been reported that the organic MA^+ and FA^+ cations of a perovskite form a loosely-bound hydrogen bond between the organic cations and the PbI_2 ionic cages. This leads to the discharge of the MA and FA species from the crystal lattice at the perovskite GBs, causing abrupt degradation.[19,23] We assume that PMMA with borax additives fills the GBs, forming complexes with dative bonds between the perovskites and the PMMA/borax.

X-ray diffraction (XRD) analysis was performed to investigate the structural orientation of the additive-embedded perovskite thin films. The diffraction peaks at 14.1°, 28.5°, and 49.9°, corresponding to the (110), (220), and (330) planes, respectively, originate from the vertical growth of the thin film. On the other hand, those at 24.4°, 31.66°, and 40.3°, attributed to the (211), (310), and (224) planes, respectively, are related to the lateral growth of the films containing the PMMA/borax additives in Figure 1B. We evaluated lateral growth of perovskite film by using full width at half maximum (FWHM) of perovskite (110) diffraction peak, as shown in Figure S1. The FWHM value of PMMA/borax samples (0.092) is 1.63 times smaller than that of the reference sample (0.15), indicating the larger grain size of the PMMA/borax sample than the reference sample, which is consistent with SEM images in the Figure 1C. It indicates that PMMA/borax can induce the grain orientation among the cross-linked perovskite grain.

To confirm the lateral growth of the perovskite film, we observed the changes in perovskite film morphology as borax concentrations were increased, as shown in Figure 1C. The reference film exhibited a grain size of 203 ± 96 nm. In contrast, the PMMA/borax-treated perovskite films have a larger grain size of 485 ± 184 nm, 542 ± 242 nm, and 675 ± 175 nm for borax concentrations of 0.5, 1.0, and 2.0 mg/mL, respectively ([PMMA] = 0.3 mg/mL, [borax] = 0.5–2.0 mg/mL). Beyond these enlarged grain growth, the bonding between $MA^+(FA^+)$, the PMMA polymer, and borax salts slows down the perovskite crystallization process.[24] Furthermore, carbonyl groups in PMMA at the boundaries will target the under-coordinated Pb^{2+}, contributing to the formation of larger grains that will merge via cross-linking.[4] Interestingly, the GBs of the perovskite film are gradually blurred as the borax concentrations increase, implying the formation of perovskite–polymer hybrid films. In addition, Figure S3 shows that the borax concentration does not affect the perovskite film thickness owing to the adoption of the same perovskite precursor concentration.

FTIR spectroscopic measurements were conducted to elucidate the effect of borax salt on the perovskite layer, as shown in Figure 1D. We found that the peak at ~1700 cm^{-1} is originated from C=N stretching vibration of FA^+. Interestingly, we observed that the C=N stretching peak was changed from 1711 cm^{-1} to 1715 cm^{-1} with an increase in the borax concentrations, which the blue-shift was attributed to the interaction of PMMA/borax with the amino group of formamidinium (FA^+). In addition, B-O bonding peak at 1510 cm^{-1} became stronger and C-H bending vibration peak was shifted from 1352 cm^{-1} to 1373 cm^{-1} with increasing in the borax concentrations, indicating that B-O-H or B-O-C bonding is promoted by the interaction between sodium borax and CH_3.[25–28] Our previous study using the proton nuclear magnetic resonance indicated that the presence of PMMA in the perovskite leads to the formation of hydrogen bonds between PMMA and perovskite.[22] Specifically, the interaction between the dipole moment of MA^+ ($CH_3NH_3^+$) in perovskite and the polar C=O bond in PMMA promoted hydrogen bond formation. Additionally, sodium tetraborate is composed of oxygen atoms bonded to boron atoms, where each boron atom is surrounded by either a triangular or tetrahedral configuration of the neighboring oxygen atoms. In this case, additional hydrogen bonds with MA^+ ($CH_3NH_3^+$) in perovskite

are likely to be formed with oxygens bonded to the boron atoms. Moreover, distinct quadruple FTIR peaks appear at 3265, 3327, 3356, and 3406 cm^{-1} that correspond to the N–H stretching vibration peaks of the FA^+ cations. Remarkably, the quadruple N–H stretching peak becomes prominent with increasing borax concentration, providing clear evidence that the addition of borax to the perovskite enhanced hydrogen bond generation.[29]

To investigate the cross-linking behavior and crystal growth mechanism, TEM images of the prepared bare perovskite film and PMMA/borax-treated films are demonstrated in Figure 1E and S2. Figure 1E shows the GBs of the bare and perovskite–polymer hybrid films with borax, revealing a polymer-dominant phase (light-colored area) between the perovskite grains (dark- colored area). The highlighted regions in Figure 1E (inside yellow dashed line) represent the polymer-dominant regions with the amorphous regions at the GBs, indicating that the PMMA polymer was predominantly located at the GBs rather than embedded into the perovskite lattice (Figure S2).[30] However, the boron ions were detected throughout the thin film area by energy-dispersive X-ray spectroscopy mapping (Figure 1E, Table S1), indicating that the interaction between the PMMA/borax mixture and perovskite crystals existed at the GBs and whole surface of the thin films. The inter-planar spacing of 3.1 Å for the reference and PMMA/borax samples (Figure S2) corresponded well to the (220) reflection of the cubic perovskite as determined via fast Fourier transform analysis and Fourier mask filtering method. These results for the (220) plane are in good agreement with that obtained from the XRD analysis.[24,31]

We fabricated PSCs, each with an n-i-p planar heterojunction architecture, with various borax concentrations

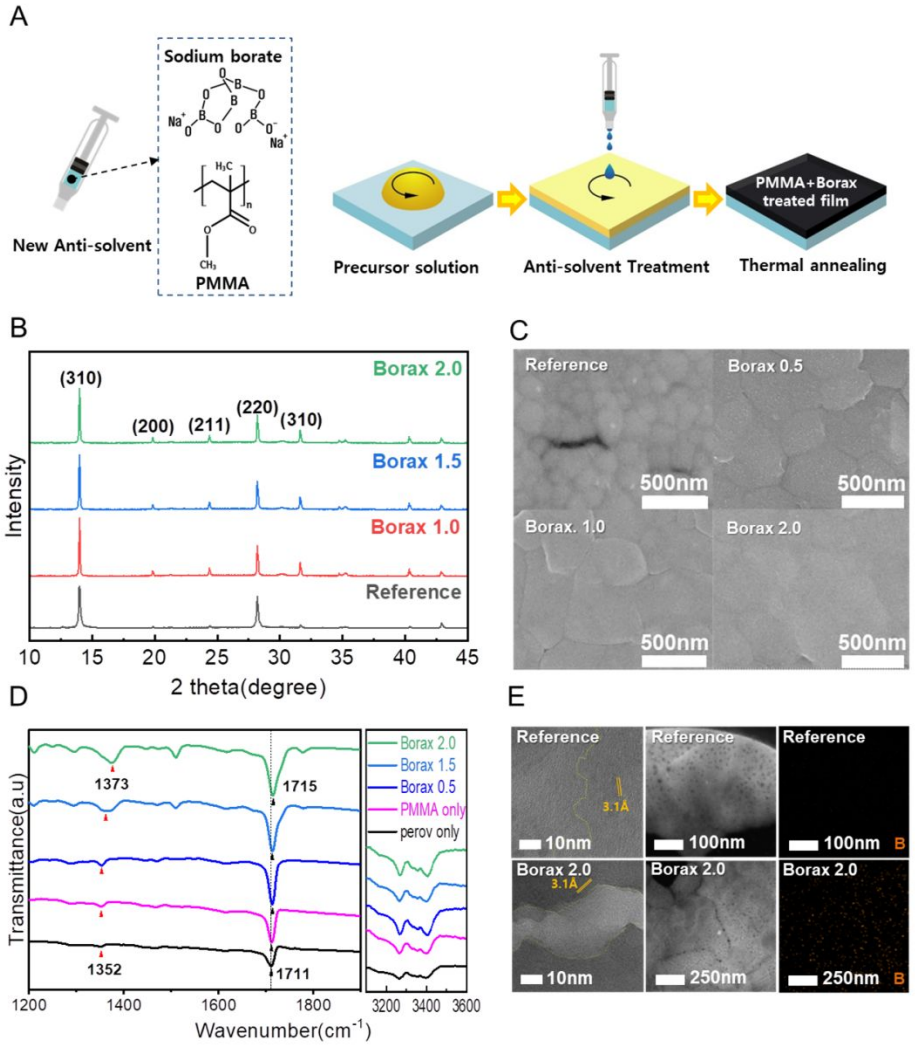

Figure 1 A. Fabrication of the PMMA/borax-embedded perovskite film. **B.** XRD data of the reference, PMMA/borax (1.0 mg/mL), PMMA/borax (1.5 mg/mL), and PMMA/borax (2.0 mg/mL) samples. **C.** Top FESEM images of the reference and PMMA/borax-embedded perovskite film. **D.** FTIR spectra of the perovskite layer only, perovskite with PMMA,

perovskite with PMMA (0.3 mg/mL) + borax (0.5 mg/mL), perovskite with PMMA (0.3 mg/mL) + borax (1.5 mg/mL), and with PMMA (0.3 mg/mL) + borax (2.0 mg/mL) on Si wafer substrates. **E.** TEM images of the GBs of the reference and PMMA/borax perovskite films.

to investigate the effect of borax salts on photovoltaic parameters. To elucidate the advantage of anti-solvent treated device, we fabricated the post-treated perovskite film using same PMMA/borax solution for comparison. Figure S4 shows the J-V curves of reference and borax-embedded PSCs. The J_{SC} was increased with PMMA/borax post treatment, while the V_{OC} and fill factor not much affect. By comparison performance By comparison performance data between anti-solvent treated device and post-treated device, PMMA/borax additives with anti-solvent can significantly passivate not only near-surface defects but also perovskite film inside. The anti-solvent dripping method can penetrate the additives into perovskite film inside because wet perovskite film is not completely crystallized. The gradient distribution of additives in perovskite film was investigated by TOF-SIMS (Time-of-Flight Secondary Ion Mass Spectrometry) analysis.[32] In addition, PMMA/borax can control the crystallization process of perovskite film via anti-solvent dripping method, exhibiting fully covered morphology with smooth surface.[33] As a result, anti-solvent treated device improved the photovoltaic performance with enhanced J_{SC}, V_{OC}, and fill factor, respectively.

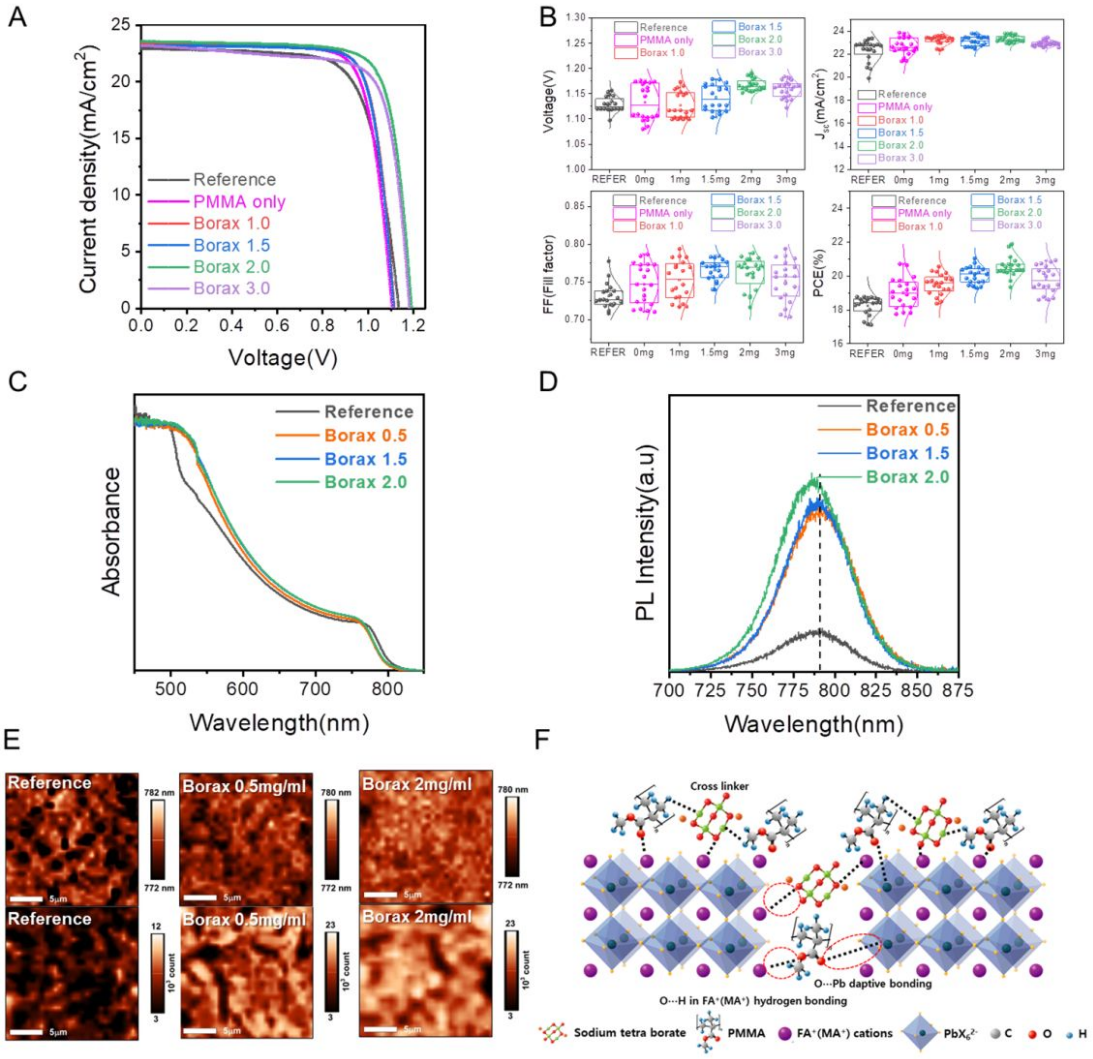

Figure 2 A. J–V curves of the reference and borax-embedded PSCs (0.5–3.0 mg/mL) with a configuration of ITO/SnO_2/perovskite/spiro/Ag. All the data were measured at AM 1.5 G (100 mW cm^{-2} intensity), **B.** Statistical box charts for the photovoltaic parameters of V_{OC}, J_{SC}, FF, and PCE of the devices having different concentrations of borax (0.5–3.0 mg/mL), **C.** Absorbance data of the perovskite layer with various concentrations of borax (0–2.0 mg/mL), **D.** Steady-state PL data of the perovskite layer with various concentrations of borax (0–2.0 mg/mL), **E.** PL mapping data of the reference sample, additive-embedded sample with PMMA (0.3 mg/mL) + borax (0.5 mg/mL), and PMMA (0.3 mg/mL) + borax (2.0

mg/mL). PL intensity distribution at specific wavelengths, showing the average fluorescence intensity of the reference, additive-embedded sample with PMMA (0.3 mg/mL) + borax (0.5 mg/mL), and PMMA (0.3 mg/mL) + borax (2.0 mg/mL) samples. Each sample has a Si/perovskite configuration, **F.** Plausible bonding configuration schemes for the PMMA/borax-treated perovskites.

In Figure 2A, the current density–voltage (J–V) characteristics of the best performing devices with various concentrations of borax (reference, PMMA-only, PMMA/borax) are depicted; these devices were fabricated with the FTO/SnO_2/perovskite/spiro-OMeTAD/Au configuration, photovoltaic parameters of each device are summarized in Figure 2B. Furthermore, the average and best performing photovoltaic characteristics of the solar cells under various conditions are summarized in Table 1. Noticeable improvements are observed in all the parameters (open-circuit voltage (V_{OC}), short-circuit current density (J_{SC}), and fill factor (FF)) of the target device (PMMA (0.3 mg/mL) + borax (2.0 mg/mL)).

The best PCE of the borax passivated device is 22.05%, with a V_{OC} of 1.19 V; JSC of 23.76 mA cm^{-2}; and FF of 78%, exhibiting a significant increase of 50 mV in the V_{OC} and 6.0% in FF. A similar trend is observed in the average V_{OC}, which increases from 1.13 to 1.17 V; the average J_{SC}, which increases from 22.31 to 23.28 mA cm^{-2}; and FF, which increases from 0.73 to 0.76, due to the retarded charge recombination induced by the passivation of the GBs and surface defects.[23] In addition, the standard deviation of J_{SC} was gradually decreased with an increase in the borax concentration, due to the uniform and large grain size of perovskite film with a smooth surface, as shown in Figure 1C. In addition, the PMMA/borax 2.0 devices exhibited extraordinary tiny deviations of V_{OC}, indicating that PMMA/borax 2.0 concentration can form uniform passivation by efficient interaction with perovskite surface and grain boundary.

As the borax concentration exceeded 2.0 mg/mL, the photovoltaic parameters showed a slightly downward tendency. A borax concentration above 2.0 mg/mL might result in an excess of Na^+ ions at the interface, resulting in smaller grain sizes and disordered grain formation, as depicted in Figure S5, significantly degrading the PSC performance.[34] The integrated J_{SC} values obtained from the external quantum efficiencies (EQEs) of the borax-embedded PSCs are in good agreement with those obtained from the J-V curve, as shown in Figure S6. Furthermore, the maximum power point results also correspond to those obtained from the aforementioned J-V results, indicating the stable operation of the device, as shown in Figure S7.

Absorption and steady-state photoluminescence (PL) measurements were performed to investigate the defect passivation behavior of the PMMA/borax-treated perovskite films. The PMMA/borax-treated perovskite films showed improved absorbance in the visible-light range, as shown by the increased surface coverage and enhanced crystal quality in Figure 2C.[35,36] In addition, the optical bandgap was slightly changed to the PMMA/borax-treated film was from 1.55 eV (reference) to 1.54 eV (PMMA/borax-treated film) due to the shifting of the Pb^{2+} 4f core-level peak.

Figure 2D shows the steady-state PL of PMMA/borax-treated film. The intensity of PL peak significantly increased with increased borax concentrations compared to reference film. Moreover, we confirmed the synergetic effects of PMMA/borax-treated film for the defect passivation, compared to the PMMA- and borax-only samples. (Figure S8).

Figure 2F shows the high-resolution PL spatial mappings of the emission spectra of the reference perovskite and PMMA/borax-treated films. The PL mappings and intensity distribution of the reference perovskite film show many dark regions, indicating that the reference films contained numerous strong PL-quenching areas, which could be in part attributed to nonradiative trap centers. Notably, as the borax concentration increases from 0 to 2.0 mg/mL, the dark regions in the PL mapping gradually disappear, leading to a uniform PL distribution as shown in Figure 2F. Furthermore, a drastic improvement in the PL intensity of the perovskite films is observed as the borax additive concentration increases from 0 to 2.0 mg/mL. Clearly, these PL mappings suggest that the addition of borax facilitates the fabrication of perovskite films with improved optical qualities. In Figure 2G, we illustrated the schematic chemical bonding structure of the perovskite and PMMA/borax blends, showing the possible interactions between the branched PMMA/borax mixture and organic $MA^+(FA^+)$ cations of $(FAPbI_3)_{0.95}(MAPbBr_3)_{0.05}$. The organic cations were bonded with PMMA and tetraborate ions by hydrogen bonding. The lone-electron pairs of the oxygen atoms in the carbonate group(C=O) from PMMA coordinate with Pb^{2+}, forming a dative bond.[37] In addition, borax acts as a cross-linker with PMMA, reacting with diols on the polymer chains to form intermolecular cross-links.[38,39] These links cover the perovskite surface and GBs. The cross-linked PMMA/borax mixtures play a role as an oxygen and moisture barrier. Hence, the PMMA/borax-treated films show great potential for stable PSCs against environmental stimuli.[40]

Table 1 Parameters of the PSCs with various borax concentrations were measured from the J–V characteristic curves. Values in parentheses are from the best performing devices

(mg/mL)	J_{SC}(mA cm^{-2})	V_{OC} (V)	FF	PCE (%)
PMMA-only	22.68 (23.85)	1.13 (1.17)	0.75 (0.75)	19.22 (20.93)
PMMA/borax 1.0	23.20 (23.49)	1.13 (1.17)	0.75 (0.74)	19.66 (20.34)
PMMA/borax 1.5	23.13 (23.05)	1.14 (1.18)	0.77 (0.78)	20.30 (21.21)
PMMA/borax 2.0	23.28 (23.76)	1.17 (1.19)	0.76 (0.78)	20.70 (22.05)
PMMA/borax 3.0	22.91 (23.43)	1.16 (1.17)	0.75 (0.76)	19.93 (20.83)

Figure 3A represents the Mott–Schottky plots (C^{-2}–V) of the devices with and without PMMA/borax treatment. The built-in potential (V_{bi}) values were calculated using the following

equation: $C^{-2} = 2(V_{bi}–V)(A^2e\varepsilon\varepsilon_oN_A)^{-1}$, where A is the active device area, and N_A is the doping concentration.[41] The V_{bi} of the device increases from 0.940 to 1.028 V for the reference and PMMA/borax 2.0 sample, respectively. To further understand the defect passivation effects of the PMMA/borax treatment, the space-charge-limited current (SCLC) was measured, as shown in Figure 3B. The trap-filled limit voltage (V_{TFL}) was calculated using the following equation: $S_{trap} = 2\varepsilon\varepsilon_oV_{TFL}/(eL^2)$, where L is the thickness of the perovskite film (500 nm); e is the elementary charge of 1.6×10^{-19}; ε is the relative dielectric constant of the mixed perovskite (≈ 32);[42] and ε_o is the vacuum permittivity (= 8.854×10^{-12} F m^{-1}). The calculated trap density of the perovskite film decreased from 3.79×10^{14} cm^{-3} (reference sample) to 3.28×10^{14} (borax 1.0) and 2.58×10^{14} cm^{-3} (borax 2.0), successfully removing the trap states in the perovskite films.

To understand the recombination behavior and charge carrier dynamics of the PMMA/borax-treated perovskite films, time-resolved photoluminescence (TRPL) measurements and fluorescence lifetime imaging (FLIM) were performed. Through FLIM, the charge carrier lifetimes of the samples with the device configuration of glass/ITO/perovskite were obtained. The lifetime of the PMMA/borax-treated film (borax 2.0) was calculated to be 122 ns, substantially longer than that of the reference film (31 ns), as shown in Figure 3C and Table S2. These TRPL results reveal efficient defect healing at the perovskite surface by the intramolecular bonding between the perovskite and PMMA/borax mixture in the thin film, proved by the effective suppression of the electron–hole recombination. The FLIM results from Figure 3D to 3I show the longer lifespans of the PMMA/borax-treated perovskite layers and the enhanced average fluorescence intensity. These figures show a sequential increment of the lifetime as indicated by the color change in the pixels (from black/dark green pixels to yellow/red pixels), corresponding to the lifetime difference obtained from the total counts of the luminescence events at each pixel.[43,44] The FLIM results demonstrate that the incorporation of borax salts enables the reduction of the nonradiative recombination pathways in perovskite film. This reduction is also related to the lower trap density and higher V_{bi} results, exhibiting increased efficiencies as the borax concentration increases.[44]

To examine the long-term air stability, non-encapsulated PCEs of the PSCs with and without the PMMA/borax treatment were recorded under ambient conditions at 22 °C and less than 10% RH for 45 days. As shown in Figure 4A, the PMMA/borax- treated PSC shows superior long-term stability, maintaining approximately 90% (average) of its initial PCE. In contrast, the untreated devices retained only 66% (average) of their initial PCEs during the same period. We expect the enhanced confinement effect produced by the strong intermolecular bonding of the perovskite layer at the GBs to prevent the

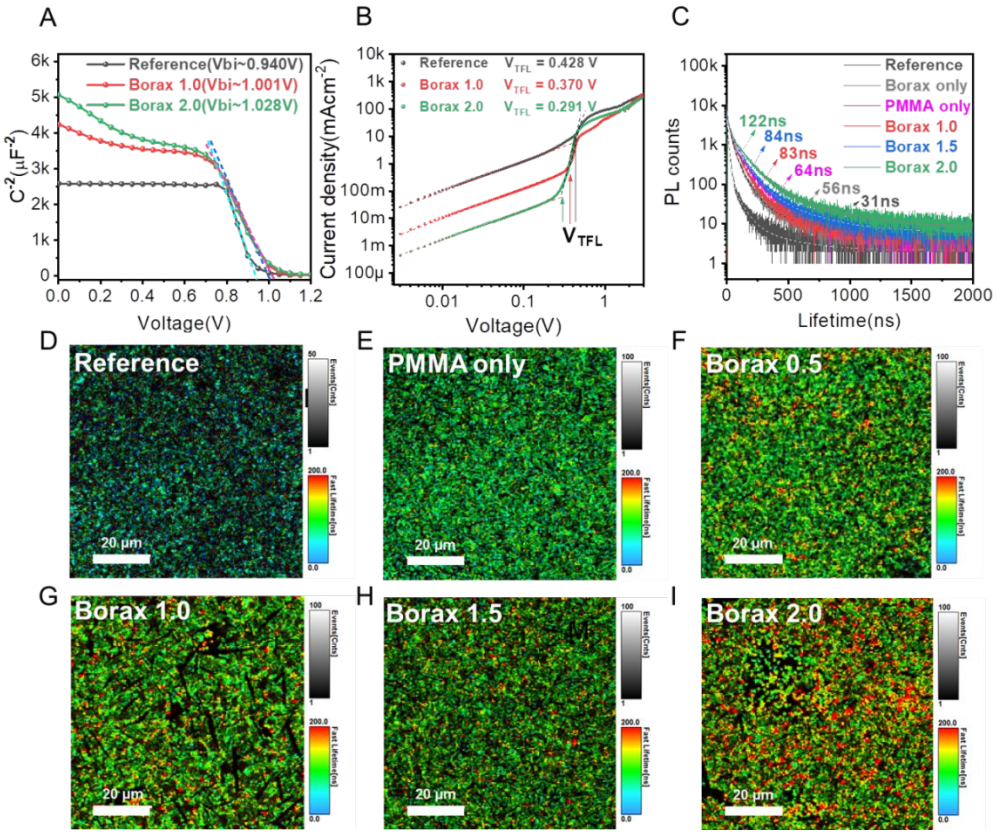

Figure 3 A. Mott–Schottky plots of the PSCs with different borax concentrations (0–2.0 mg/mL) under dark condition, **B.** Dark J–V curves of the electron-only devices (ITO/SnO_2/perovskite/PCBM/Ag) having different concentrations of borax at a frequency of 1 kHz, **C.** Sequential lifetime increment measured by TRPL (borax-only < PMMA-only (0.3 mg/mL) < PMMA (0.3 mg/mL)/borax (0.5 mg/mL) < PMMA (0.3 mg/mL)/borax (1.5 mg/mL) < PMMA (0.3 mg/mL)/borax (2 mg/mL). FLIM results of **D.** reference sample, **E.** PMMA-only sample (0.3 mg/mL), **F.** PMMA (0.3 mg/mL)/borax (0.5 mg/mL) sample, **G.** PMMA (0.3 mg/mL)/borax (1 mg/mL) sample, **H.** PMMA (0.3 mg/mL)/borax (1.5 mg/mL) sample, and **I.** PMMA (0.3 mg/mL)/borax (2 mg/mL) sample.

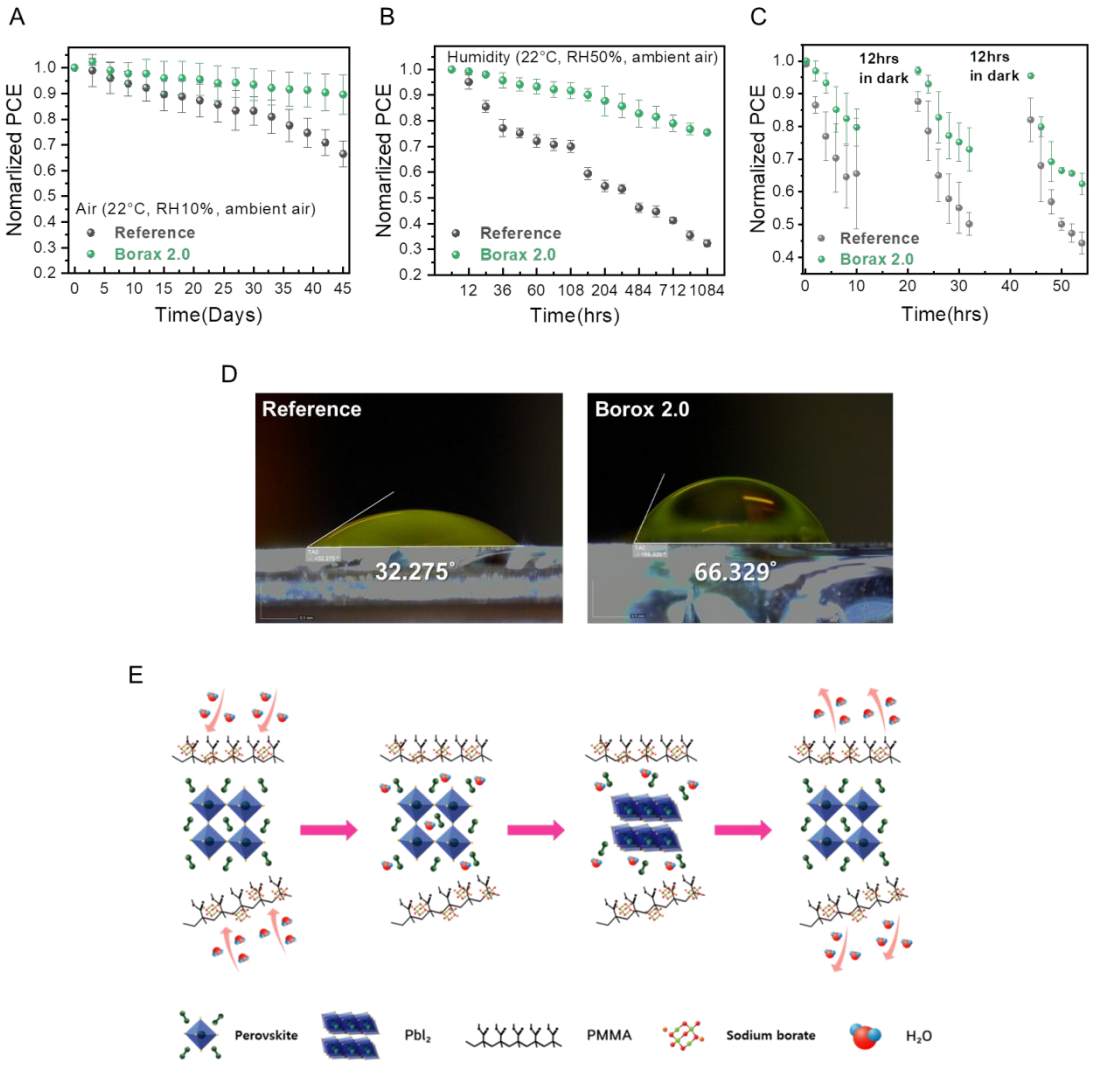

Figure 4 A. Air stability test in ambient condition (room temperature and less than 10% RH). **B.** Stability test results of the reference and PMMA/borax-treated samples, obtained, under 50% RH. **C.** Comparison of light stability between the reference and PMMA/borax-treated samples. **D.** Contact angles of deionized water droplets on the reference and PMMA (0.3 mg/mL)/borax (2.0 mg/mL) samples. **E.** Mechanistic scheme of the self-healing blended layer.

leakage of the decomposed intermediates from the perovskite film to the outside environment, thereby improving the stability of the PMMA/borax-treated devices. The moisture stability of the devices was examined by exposing the as-prepared samples with and without borax treatment to 22 °C and 50% RH for 1084 h, as shown in Figure 4B. The PMMA/borax-treated devices exhibited superior moisture stability by retaining ~80% of their initial PCEs, whereas the reference devices show only 32% of their original state after 1084h. Furthermore, the hydroscopic behavior of the PMMMA/borax-treated samples was confirmed via contact angle measurements. As shown in Figure 4D, 4E, and S11, the contact angle of the deionized water droplets on the reference perovskite is 32.3°, much lower than that of the PMMA/borax-

treated sample (66.3°; 2.0 mg/mL) after 30 s. Interestingly, the PMMA-only and borax-only treated samples showed contact angles of 48.6° and 50.7°, respectively. These values indicate the superior cross-linking behavior between the PMMA and borax on the borax-embedded perovskite films. A similar tendency is observed in Figure S12, indicating that compared to the reference and PMMA-only thin films, the PMMA/borax-treated perovskite thin films maintain their phase with minimal degradation in ambient conditions at 22 °C, 20 ± 10% RH after 30 days. In addition, the photostability recovery of the reference and PMMA/borax-treated perovskite films were investigated, and the corresponding results are shown in molecules, then 2) the FAI or MAI species are strongly bonded by the PMMA/borax mixture such that the decomposed intermediate species cannot escape and instead react with PbI_2 to regenerate the perovskite phase.[45] Thus, the borax salts were utilized for making dense "confinement cages" to promote the self-healing process in the blended perovskite films with PMMA/borax. This decomposition-regeneration mechanism explains the improved stability and self-healing effect in the PMMA/borax-treated perovskite film. And the comprehensive understanding the role of PMMA/borax additives will help researchers to adopt rational use and design of additives for solving stability issues of various perovskite based optoelectronic applications.

3. Conclusions

In this study, we investigated the effect of adding PMMA/sodium borate in perovskite films by employing an anti-solvent dripping method. This process provided unique features that enhanced the hydrogen bond formation between the PMMA/sodium borate mixture and perovskite, changing the crystal growth direction and surface morphology and significantly improving device performance and stability. The strong binding by hydrogen bonding enabled both superior passivation and retardation of the phase decomposition process in the perovskite absorber. Finally, it facilitated the recrystallization of the film, resulting in improved solar cell performance. The non-encapsulated PMMA/sodium borate-embedded device showed excellent stability in the air, retaining over 90% of its initial efficiency over 45 d (averaged 20.52%). Additionally, it demonstrated remarkable reproducibility in humid conditions, maintaining 80% of the device performance over 1084 h at 22 ℃ and 50% RH. We believe that this technology will significantly contribute to the commercialization of various optoelectronic devices such as photovoltaics, photodetectors, and light-emitting diodes.

4. Experimental section

4.1 Materials

Indium tin oxide (ITO) was supplied by Hanalintech (Republic of Korea, ROK). Ethyl alcohol (EtOH, 99.5%), and acetone (99.5%) were purchased from DaeJung Chemicals & Metals (ROK). Tin (IV) oxide (c-SnO2, 15% in H_2O colloidal dispersion) Figure 4C. We measured the PCE of each device exposed to 1 sun illumination for 10 h by recording the PCE every 2 h under ambient conditions (22–25 °C, 45–55% RH). After resting for 12 h in dark conditions (in a glovebox with Ar atmosphere, 22–23 °C), the PMMA/borax-treated perovskite PSCs recovered from their degraded states to their initial states, retaining over 95% of their initial PCEs after 44 h exposure. In contrast, the reference device showed retarded healing, recovering at most 80% of its initial PCE after the same period.

The mechanistic processes are illustrated in Figure 4E; 1) PMMA/borax forms a dense moisture barrier to prevent moisture penetration into the thin film, by absorbing the water was purchased from Alfa Aesar (USA). Hellmanex III (detergent), Polymethylmethacrylate (PMMA, Mw~15,000), cesium iodide (99.9%), ethyl acetate(99.8%), N,N-dimethylformamide (DMF, 99.8%), dimethyl sulfoxide (DMSO, 99.9%), anisole (anhydrous, 99.7%), toluene (99.8%), chlorobenzene (99.8%), 4-tert-butyl pyridine (tBP, 98%), acetonitrile (99.8%), and bis(trifluoromethane)sulfonimide lithium salt (Li-TFSI, 99.95%) were purchased from Sigma-Aldrich (USA). Formamidinium iodide (99.9%), methylammonium bromide (99.9%), and methylammonium chloride (MACl, 98%) were purchased from GreatCell Solar (Australia). The 2,2',7,7'-tetrakis (N,N-di-p-methoxyphenylamine)-9,9'-spirobifluorene (Spiro-OMeTAD, LT-S922) was purchased from the Luminescence Technology Corp. Poly[bis (4-phenyl)(2,4,6-trimethylphenyl)amine] (PTAA, Mn = 3200, Mw = 4900) was purchased from Xi'an Polymer Light Technology Corp (China). All materials were used as received without post-treatment or further purification.

4.2 Device fabrication

PSCs were fabricated on glasses coated with ITO patterned by laser etching. The etched substrates were cleaned sequentially using detergent solution (2 vol% of Hellmanex in DI water), DI water, acetone, and ethanol in an ultrasonic bath for 10 min each. Then, the cleaned substrates were treated with ultraviolet–ozone to remove residual organic contaminants and enhance the wettability of the resulting hole-transporting layer over 30 min. Next, a SnO_2 nanoparticle solution (c-SnO_2: DI-water=1:3 volume ratio) was spun on the ITO layer (at 3000 rpm for 30 s), and the coated substrate was annealed at 100 °C for 10 min. Then, 1.6 M $(FAPbI_3)_{0.95}(MAPbBr_3)_{0.05}$ perovskite precursor solutions were prepared by dissolving corresponding amounts of FAI (0.263 g), MABr (0.009 g), PbI2 (0.726 g), PbBr2 (0.029 g), and MACl (0.035 g) in a DMSO/DMF (2:8; 1 mL) mixed solvent (with 3% molar ratio and excess PbI2). The solution was stirred at room temperature (20-22 ℃) for at least 30 min before use and filtered through a polytetrafluoroethylene filter (0.45-μm mesh).

The anti-solvent solution was prepared by dissolving PMMA (0.3 mg mL-1) in a chlorobenzene/toluene mixed solvent (9:1), followed by the addition of sodium borate salts, which were dispersed in ethyl acetate via ultrasonication over 12 h. Notably, it is very important to grind sodium borate finely with a mortar before its addition. After preparing a well-dispersed

solution, the PMMA and borax solutions were mixed in a 9:1 ratio. The perovskite layer was formed on the electron transporting layer via one-step spinning at 5000 rpm for 25 s. The substrate was treated with the anti-solvent (0.5 mL) solution by drop-casting before 20 s of spinning. The substrate was annealed on a hot plate at 150 °C for 10 min. Next, The hole transfer materials were deposited by preparing Spiro-OMeTAD in chlorobenzene (90 mg/mL) and mixing with 39 µL 4-tertbutylpyridine (tBP), 23 µL Li-TFSI (520 mg/ mL in acetonitrile), and 10 µL tris[2-(1H-pyrazol1-yl)-4-tert-butylpyridine]-cobalt(III)-tris[bis-(trifluoromethylsulfonyl)imide] (FK209, great solar cell; 375 mg/mL–1 acetonitrile). In the last stage, the samples were transferred into a thermal evaporator, and a 100-nm-thick Ag layer was deposited at a pressure of 5×10^{-6} Torr to develop devices with ITO/SnO_2/perovskite/spiro-OMeTAD/Ag configurations.

4.3 Device characterization

The J–V characteristics of the prepared solar cells were measured using a solar simulator (Newport Oriel Solar 3A Class AAA, 64023A) and a potentiostat (CHI 660D, CH instruments) under the illumination of an AM 1.5 G spectrum (100 mA cm^{-2}). The potentiostat was calibrated using a standard Si solar cell (Oriel, VLSI standards) and a light sensor current controller (Newport Oriel digital exposure controller, Model 68945). All the devices were tested by masking their active areas with a thin mask (0.14 cm^2). The J–V curves were recorded at a scan rate of 300 mV s^{-1} under AM 1.5G (100 mW cm^{-2}) conditions at room temperature (22-23 ℃) with less than 10% RH. The EQE values were measured in the short-circuit condition using a solar simulator (ABET Technology 10500 solar simulator) as the light source and a light solution (SPECTRO Mmac-200).

The TRPL curves were recorded using a commercial TCSPC system (FluoTime 200, PicoQuant). The samples were excited using a 670-nm picosecond diode laser (LDH-P-C-670, PicoQuant) with a repetition rate of 4 MHz. The emitted PL signal was accumulated using a fast photomultiplier tube detector (PMA 182, PicoQuant) with a magic angle (54.7°) arrangement. The incident angle of the excitation pulse was set at ~30° with respect to the sample. The resulting instrumental response function was 160 ps (full width at half maximum). The PL decays were measured at the emission peak (770 nm) of the perovskite. In addition, a cut-off filter (FF01-692 nm, Semrock) was applied to block the scattering. The FLIM measurements were conducted using an inverted-type scanning confocal microscope (SP8 FALCON, Leica Microsystems, Germany) with a 100× (oil) objective lens. A 535-nm picosecond laser line from a white-light laser source was used as the excitation source. A hybrid photon detector was used to detect the emitted radiations from the samples. Fluorescence confocal and lifetime images of 512 pixels × 512 pixels were simultaneously recorded using a galvo-stage and time-correlated single-photon counting technique. The obtained fluorescence decays were fitted with an exponential function using the Leica suited software (LAS X Ver.3.5.2).

For FTIR spectroscopy, the samples were prepared with the c-Si/perovskite configuration. Their FTIR spectra were recorded using a Nicolet 5700 instrument (Thermofisher Scientific, USA) from 4000 to 400 cm^{-1} with a resolution of 4 cm^{-1}.

The XRD patterns were collected via an Ultima III (Rigaku) diffractometer using Cu Kα radiation by step scanning at a scanning speed of 4° min^{-1}, from 5° to 60°. The 2θ scans were obtained from the perovskite samples deposited on the ITO glasses.

Author Contributions

B.J. and G.S.H. contributed equally to this work. G. N., T.K.A., and H.S.J. supervised the project. B.J. conceived the idea, designed all experiments and analyzed data. H.M. Y performed PL mapping, and FLIM. J.C. performed XRD experiment to check the crystallization. G.S.H. and J. Z. provided helpful discussions for paper writing. All authors made substantial contributions to the discussion of the content and reviewed and edited the manuscript before submission. B.J., G.S.H., H.S.J. and G.N. wrote the manuscript with input from all authors.

Conflicts of interest

There are no conflicts to declare.

Acknowledgements

This research was supported by the Future Materials Discovery Program (2019M3D1A2104108), and the Korea Institute of Energy Technology Evaluation and Planning (KETEP) grant funded by the Korean Government (MOTIE) (No. 20203040010320).

This work is also partially supported by the National Research Foundation of Korea (NRF) grant funded by the Korea Government (2020R1I1A1A01063958), the Brain Pool Program (the 2020H1D3A2A01064555), and the National Science Foundation (under project no. 1547771).

Notes and references

1 W. Chen, Y. Wang, G. Pang, C. W. Koh, A. B. Djurišić, Y. Wu, B. Tu, F. zhou Liu, R. Chen, H. Y. Woo, X. Guo and Z. He, *Adv. Funct. Mater.*, 2019, **29**, 1–10.

2 M. Kim, J. Jeong, H. Lu, T. K. Lee, F. T. Eickemeyer, Y. Liu, I. W. Choi, S. J. Choi, Y. Jo, H. B. Kim, S. I. Mo, Y. K. Kim, H. Lee, N. G. An, S. Cho, W. R. Tress, S. M. Zakeeruddin, A. Hagfeldt, J. Y. Kim, M. Grätzel and D. S. Kim, *Science (80-.).*, 2022, **375**, 302–306.

3 J. M. Ball and A. Petrozza, *Nat. Energy*, 2016, **1**, 16149.

4 J. Jiang, Q. Wang, Z. Jin, X. Zhang, J. Lei, H. Bin, Z. G. Zhang, Y. Li and S. F. Liu, *Adv. Energy Mater.*, 2018, **8**, 1–9.

5 S. Ahmad, P. Fu, S. Yu, Q. Yang, X. Liu, X. Wang, X. Wang, X. Guo and C. Li, *Joule*, 2019, **3**, 794–806.

6 T. Wu, Z. Qin, Y. Wang, Y. Wu, W. Chen, S. Zhang, M. Cai, S. Dai, J. Zhang, J. Liu, Z. Zhou, X. Liu, H. Segawa, H. Tan, Q. Tang, J. Fang, Y. Li, L. Ding, Z. Ning, Y. Qi, Y. Zhang and L. Han, *Nano-Micro Lett.*, 2021, **13**, 1–18.

7 F. Yu, J. Liu, J. Huang, P. Xu, C. H. Li, Y. X. Zheng, H. Tan and J. L. Zuo, *Sol. RRL*, 2022, **6**, 1–7.

8 Y. Mei, M. Sun, H. Liu, X. Li and S. Wang, *Org. Electron.*, 2021, **96**, 106258.

9 L. K. Ono, E. J. Juarez-Perez and Y. Qi, *ACS Appl. Mater. Interfaces*, 2017, **9**, 30197–30246.

10 Y. Sun, Y. Wu, X. Fang, L. Xu, Z. Ma, Y. Lu, W. H. Zhang, Q. Yu, N. Yuan and J. Ding, *J. Mater. Chem. A*, 2017, **5**, 1374–1379.

11 C. Li, A. Wang, L. Xie, X. Deng, K. Liao, J. A. Yang, T. Li and F. Hao, *J. Mater. Chem. A*, 2019, **7**, 24150–24163.

12 J. Chang, Z. Lin, H. Zhu, F. H. Isikgor, Q. H. Xu, C. Zhang, Y. Hao and J. Ouyang, *J. Mater. Chem. A*, 2016, **4**, 16546–16552.

13 X. Meng, J. Lin, X. Liu, X. He, Y. Wang, T. Noda, T. Wu, X. Yang and L. Han, *Adv. Mater.*, 2019, **31**, 1–7.

14 Y. Zhao, J. Wei, H. Li, Y. Yan, W. Zhou, D. Yu and Q. Zhao, *Nat. Commun.*, 2016, **7**, 1–9.

15 H. P. Kim, A. R. Bin Mohd Yusoff and J. Jang, *Nanoscale Adv.*, 2019, **1**, 76–85.

16 S. Tian, J. Chen, X. Lian, Y. Wang, Y. Zhang, W. Yang, G. Wu, W. Qiu and H. Chen, *J. Mater. Chem. A*, 2019, **7**, 14027–14032.

17 E. Ochoa-Martinez, M. Ochoa, R. D. Ortuso, P. Ferdowsi, R. Carron, A. N. Tiwari, U. Steiner and M. Saliba, *ACS Energy Lett.*, 2021, **6**, 2626–2634.

18 F. Yang, H. E. Lim, F. Wang, M. Ozaki, A. Shimazaki, J. Liu, N. B. Mohamed, K. Shinokita, Y. Miyauchi, A. Wakamiya, Y. Murata and K. Matsuda, *Adv. Mater. Interfaces*, 2018, **5**, 1–10.

19 P. Xu, J. Liu, J. Huang, F. Yu, C. H. Li and Y. X. Zheng, *New J. Chem.*, 2021, **45**, 13168–13174.

20 J. Zhang, L. Wan, Y. Gao, X. Fang, T. Lu, L. Pan and F. Xuan, *Adv. Electron. Mater.*, 2019, **5**, 1–10.

21 S. N. Habisreutinger, D. P. McMeekin, H. J. Snaith and R. J. Nicholas, *APL Mater.*, 2016, **4**, 1–15.

22 T. T. Ava, H. J. Jeong, H. M. Yu, K. N. Lee, T. M. Abdel-Fattah, M. S. Jeong and G. Namkoong, *Appl. Surf. Sci.*, 2021, **558**, 149852.

23 Q. Cao, Y. Li, H. Zhang, J. Yang, J. Han, T. Xu, S. Wang, Z. Wang, B. Gao, J. Zhao, X. Li, X. Ma, S. M. Zakeeruddin, W. E. I. Sha, X. Li and M. Grätzel, *Sci. Adv.*, 2021, **7**, 1–12.

24 T. H. Han, J. W. Lee, C. Choi, S. Tan, C. Lee, Y. Zhao, Z. Dai, N. De Marco, S. J. Lee, S. H. Bae, Y. Yuan, H. M. Lee, Y. Huang and Y. Yang, *Nat. Commun.*, 2019, **10**, 1–10.

25 S. Mondal and A. K. Banthia, *J. Eur. Ceram. Soc.*, 2005, **25**, 287–291.

26 M. Huang, Y. Hou, Y. Li, D. Wang and L. Zhang, *Des. Monomers Polym.*, 2017, **20**, 505–513.

27 Y. Zheng, Y. Cui and W. Wang, *Minerals.*, 2018, **8**, 341.

28 A. C. Ersan, A. S. Kipcak, M. Y. Ozen and N. Tugrul, *Main Gr. Met. Chem.*, 2020, **43**, 7–14.

29 F. C. Wang, M. Feve, T. M. Lam and J. -P Pascault, *J. Polym. Sci. Part B Polym. Phys.*, 1994, **32**, 1315–1320.

30 X. Li, W. Zhang, Y. C. Wang, W. Zhang, H. Q. Wang and J. Fang, *Nat. Commun.*, 2018, **9**, 1–10.

31 Y. Zhang, X. Hu, L. Chen, Z. Huang, Q. Fu, Y. Liu, L. Zhang and Y. Chen, *Org. Electron.*, 2016, **30**, 281–288.

32 Y.-J. Kang and S.-I. Na, *Nano Energy*, 2022, **97**, 107193.

33 A. D. Taylor, Q. Sun, K. P. Goetz, Q. An, T. Schramm, Y. Hofstetter, M. Litterst, F. Paulus and Y. Vaynzof, *Nat. Commun.*, 2021, **12**, 1–11.

34 L. Wang, D. Moghe, S. Hafezian, P. Chen, M. Young, M. Elinski, L. Martinu, S. Kéna-Cohen and R. R. Lunt, *ACS Appl. Mater. Interfaces*, 2016, **8**, 23086–23094.

35 A. Savva, I. T. Papadas, D. Tsikritzis, G. S. Armatas, S. Kennou and S. A. Choulis, *J. Mater. Chem. A*, 2017, **5**, 20381–20389.

36 H. Do Kim, H. Ohkita, H. Benten and S. Ito, *Adv. Mater.*, 2016, **28**, 917–922.

37 C. Wu, H. Li, Y. Yan, B. Chi, K. M. Felice, R. B. Moore, B. A. Magill, R. R. H. H. Mudiyanselage, G. A. Khodaparast, M. Sanghadasa and S. Priya, *Sol. RRL*, 2018, **2**, 1–9.

38 C. Riedo, F. Caldera, T. Poli and O. Chiantore, *Herit. Sci.*, 2015, **3**, 1–11.

39 S. Cho, S. Y. Hwang, D. X. Oh and J. Park, *J. Mater. Chem. A*, 2021, **9**, 14630–14655.

40 M. Lu, S. Huang, S. Chen, Q. Ju, M. Xiao, X. Peng, S. Wang and Y. Meng, *Polym. J.*, 2018, **50**, 239–250.

41 A. Guerrero, E. J. Juarez-Perez, J. Bisquert, I. Mora-Sero and G. Garcia-Belmonte, *Appl. Phys. Lett.*, 2014, **105**, 1–5.

42 Y. Wang, T. Mahmoudi and Y. B. Hahn, *Adv. Energy Mater.*, 2020, **10**, 1–11.

43 K. Jung, W.-S. Chae, K.-H. Lee and M.-J. Lee, *J. Mater. Res. Technol.*, 2021, **13**, 162–172.

44 K. Jung, J. H. Lee, K. Oh, C. Im, J. Do, J. Kim, W. S. Chae and M. J. Lee, *Nano Energy*, 2018, **54**, 251–263.

45 Y. Zhao, P. Zhu, M. Wang, S. Huang, Z. Zhao, S. Tan, T. Han, J. Lee, T. Huang, R. Wang, J. Xue, D. Meng, Y. Huang, J. Marian, J. Zhu and Y. Yang, 2020, **1907769**, 1–8.